The Journal of Experimental Biology 210, 881-896
Published by The Company of Biologists 2007
doi:10.1242/jeb.02704

A computational investigation of the three-dimensional unsteady aerodynamics of *Drosophila* hovering and maneuvering

Ravi Ramamurti* and William C. Sandberg

Laboratory for Computational Physics and Fluid Dynamics, Naval Research Laboratory, Washington, DC 20375, USA

*Author for correspondence (e-mail: ravi@lcp.nrl.navy.mil)

Accepted 22 December 2006

Summary

Three-dimensional unsteady computations of the flow past a fruit fly *Drosophila* under hovering and free flight conditions are computed. The kinematics of the wings and the body of the fruit fly are prescribed from experimental observations. The computed unsteady lift and thrust forces are validated with experimental results and are in excellent agreement. The unsteady aerodynamic origin of the time-varying yaw moment is identified. The differences in the kinematics between the right and the left wings show that subtle change in the stroke angle and deviation angle can result in the yaw moment for the turning maneuver. The computed yaw moment reaches a peak value at the beginning of the maneuver and remains positive throughout the remainder of the maneuver. The origin of the yaw moment is investigated by computing the center of pressures on each wing and the individual moment arms. This investigation leads to the conclusion that it is the forward force and a component of the lift force that combine to produce the turning moment while the side force alone produces the restoring torque during the maneuver. The vorticity shed from the wing's leading edge and the tips show a loop like structure that during stroke reversals pinches off into Λ-like structures that have not been previously observed in the wakes of flapping fliers.

Key words: flapping wings, insect flight, insect hovering, insect maneuvering, *Drosophila*, incompressible flow, unstructured grid, unsteady aerodynamics.

Introduction

Flapping wing locomotion and maneuvering mechanisms are of interest to behavioral biologists, biomechanics researchers, and engineers attempting to develop systems that can match the performance of living creatures. The flight dynamics of insects are quite complex. For example, the motion of the fruit fly *Drosophila melanogaster* involves several successive sharp right angle turns. These turns, called saccades, are characteristic of many insects. Understanding the three-dimensional (3-D) unsteady aerodynamics of the two flapping wings and the insect body that results in the saccade maneuver would be extremely valuable to designers in their attempts to create vehicles capable of emulating such obstacle-avoidance performance. Unlike rotary wing flight that produces a steady torque on the body, flapping flight should generate an oscillatory torque. There are numerous questions one would wish to answer before embarking on a vehicle design for saccade-like maneuvering performance. A particularly important question is 'How does the unsteady flow field about multiple flapping wings and an insect body interact and evolve to produce lift and thrust?' and secondly, 'If the flapping is asymmetric what is the instantaneous flow field and how does it evolve to produce the desired maneuvering moment?' Or to put it another way, 'How much asymmetry between multiple flapping wings is needed to achieve a specific maneuvering moment and what are the underlying aerodynamics of the moment generation?' Also, insect flight is largely in the laminar regime, with vortices being shed persistently from the leading edge and the wing tips. Understanding the role of these shed vortices on the lift and thrust development is also important.

Flapping foil propulsion has received considerable attention in the past few years as an alternative to the propeller. Experimental and computational investigations have been carried out on several fronts to gain insight into insect flight performance and use those insights in vehicle design. Kellogg et al. (Kellogg et al., 2001; Kellogg et al., 2003) and Jones and Platzer (Jones and Platzer, 2003) have experimentally investigated the use of tandem flapping foils for micro-air vehicle propulsion and were successful. Ramamurti et al. (Ramamurti et al., 2005) computationally studied the unsteady thrust and lift generation of tandem multiple flapping wing vehicles as well as rotary-wing vehicles to support MicroAirVehicle (MAV) design efforts. For these types of vehicles, it is important to accurately quantify the performance of flapping wings in order to provide the controllability needed during a maneuver.

The effects of the wing rotation have been studied in the fruit fly, *Drosophila* (Dickinson et al., 1999). 3-D unsteady flow

computations over an insect wing (Liu and Kawachi, 1998) were used to obtain qualitative agreement for the flow patterns over a hovering hawkmoth with the visualizations previously obtained in a windtunnel (Willmott and Ellington, 1997). Force production in the single flapping wing of *Drosophila* has also been studied (Ramamurti and Sandberg, 2002; Sun and Tang, 2002). Ramamurti et al. also studied the force production about the flapping and deforming pectoral fin and body of the swimming bird wrasse fish computationally (Ramamurti et al., 2002). Their experimental results provided good agreement with measured force data (Dickinson et al., 1999) and fish acceleration data (Walker and Westneat, 1997). Since one would like to know the importance of wing deformation time history to lift and thrust production time history, Ramamurti et al. investigated the fluid dynamics underlying the generation of forces during pectoral fin oscillation as fin rigidity and resulting shape deformation time history is varied (Ramamurti et al., 2004). All of these investigations focused primarily on lift and thrust production mechanisms for forward flight or straight ahead swimming.

Recently the question of force production during insect turning has been addressed. Fry et al. (Fry et al., 2003) studied the wing and body kinematics of free flying *Drosophila* performing rapid maneuvers. They measured insect wing and body kinematics and used that data to drive a robotic model of the fruit fly. They measured the total aerodynamic force and torque during the specified saccade maneuver of the fly model. The results of Fry's work indicated that inertia rather than viscous effects dominated the torque production. The details of the unsteady aerodynamics of force and yaw moment production by each of the two asymmetrically flapping wings interacting with the fly body and how those were related to the overall insect torque production was still an open question. We address that question with the computational investigation reported here.

The primary objectives of this study were to (i) computationally simulate the maneuver of the fruit fly using prescribed wing and body kinematics observed from experiments, (ii) to validate the computed forces with the experimentally measured forces, (iii) to compute the unsteady aerodynamics of force production by each asymmetrically flapping wing, and (iv) to understand the subtle changes in kinematics observed by Fry et al. (Fry et al., 2003) that lead to the net measured torque required for the maneuver. In this manner, a computational investigation can complement physical observations and measurements by providing the unsteady pressure time-histories on all moving surfaces and the detailed velocity and vorticity map of the evolving flow field associated with either measured or derived total force data. This can be of value not only to biomimetic vehicle designers but also to the biological community, since knowledge of surface pressure distribution time histories during insect, bird or fish locomotion and maneuvering is essential to understanding the bone, muscle and skin external loading experienced by these creatures as they execute such motions. The surface pressure time-histories on insect bodies and flapping wings are the crucial missing unsteady data that cannot be measured in insect free flight, and only with great difficulty on models. The biologist can now use this unsteady computed data to explore questions such as why the wing hinge joint and wing root have the shape and structure that they have. One possibility is that the shape and structure have evolved to enable the object or prey avoidance maneuvers observed and hence must be capable of supporting the wing hinge time-varying moments throughout a maneuver. That is, the insect physiology and biomechanics enable it to operate successfully in its environment.

There are many aspects to consider when investigating the insect's dynamic behavior in an unsteady environment and what is required for success. External stimuli can be optical, thermal, chemical and mechanical. Kinematics of insect responses to such stimuli can be measured by biologists and provided as input to 3-D unsteady aerodynamics computations. The resulting force and moment time histories and wake vorticity evolutions can then assist in answering functional morphology questions by providing otherwise unavailable information on what structural and dynamic characteristics the insect must possess to enable its dynamic responses. Computational investigations directed at answering morphology questions may then lead to the answers to other questions, such as whether the structure of the wing hinge joint, for example, has evolved to enable the saccade maneuver or possibly some other dynamic behavior such as stable flight in a wind gust, where an unsteady pressure field provides the external stimuli. Investigation of wind-borne chemical stimuli and subsequent dynamic responses is another area where computations can be of assistance. Examination of the geometry and location of chemical receptors in concert with the insect unsteady flight aerodynamics may provide insights into how the receptors enable successful tracking of pheromones or other chemicals of interest in a random wind-gust environment. Do the energy demands of flight in wind gusts restrict operations above a certain magnitude or is it a biomechanical limitation that dominates? There are numerous biological questions of this sort that are not answerable solely by laboratory or field measurements but on which progress can be made by complementary investigations that include the unsteady aerodynamic computations we describe below.

Materials and methods

To study the aerodynamics of the maneuvering flight, Fry et al. (Fry et al., 2003) captured the saccade of the fruit fly, *Drosphila melanogaster*, using a three high-speed video camera system. The flies were untethered and were enticed towards a target with a drop of vinegar. Some of the flies performed collision avoiding maneuvers, resulting in the measurement of the body and wing kinematics throughout the maneuver that were used in the present study.

The incompressible flow solver

The governing equations employed are the incompressible

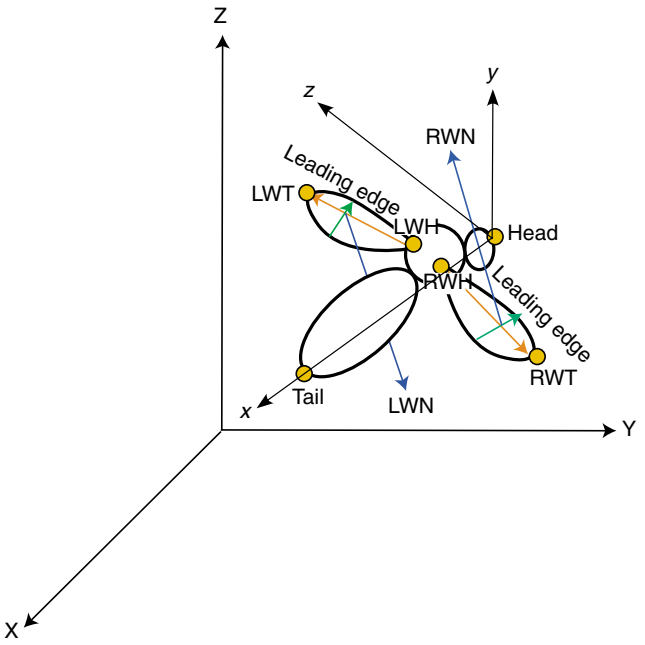

Fig. 1. Schematic of the hovering *Drosophila*. LWT, RWT, left/right wingtip; LWH, RWH, left/right wing hinge; LWN, RWN, left/right wing normal vector.

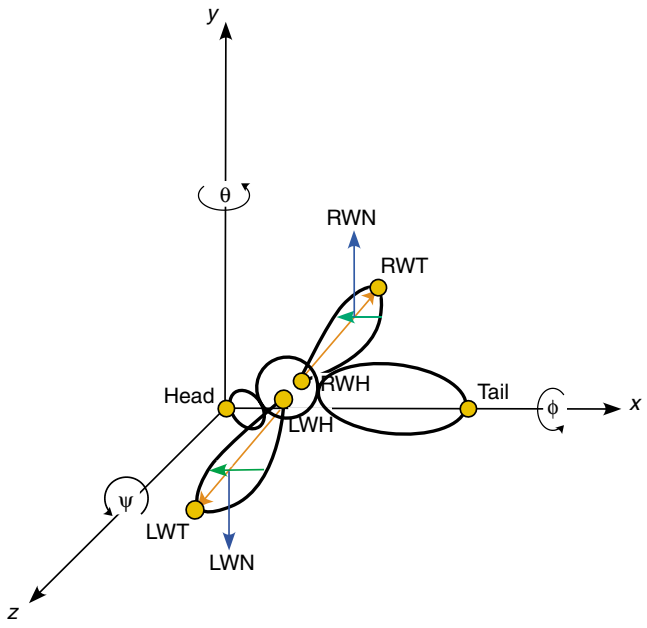

Fig. 2. Schematic of the *Drosophila* in the computational coordinate system. Abbreviations as in Fig. 1.

Navier–Stokes equations in Arbitrary Lagrangian-Eulerian (ALE), formulation which are written as:

$$\frac{\mathrm{d}\mathbf{v}}{\mathrm{d}t} + \mathbf{v}_\mathrm{a} \cdot \nabla\mathbf{v} + \nabla p = \nu\nabla^2\mathbf{v} \ , \qquad (1)$$

$$\nabla \times \mathbf{v} = 0 \ . \qquad (2)$$

In Eqn 1, p denotes the pressure, $\mathbf{v}_\mathrm{a}$=$\mathbf{v}$–$\mathbf{w}$ is the advective velocity vector, where $\mathbf{v}$ is the flow velocity and $\mathbf{w}$ is the mesh velocity and the material derivative is with respect to the mesh velocity $\mathbf{w}$. Both the pressure p and the viscous stress tensor have been normalized by the (constant) density ρ and are discretized in time using an implicit time stepping procedure. Thus the equations are Eulerian for zero mesh velocity and Lagrangian if the mesh velocity is the same as the flow velocity. The present time-accurate flow solver is discretized in space using a Galerkin procedure with linear tetrahedral elements. The details of the flow solver have already been discussed extensively elsewhere (Ramamurti and Löhner, 1992; Ramamurti et al., 1994; Ramamurti et al., 1995; Ramamurti et al., 1999) in connection with successfully validated solutions for numerous 2-D and 3-D, laminar and turbulent, steady and unsteady flow problems.

Results and discussion

The unsteady flow past an isolated *Drosophila* wing has been computed (Ramamurti and Sandberg, 2002), and the effect of phasing between the translational and rotational motions on the thrust production of a hovering fruit fly was studied. In the present study, we extend this work and compute the unsteady forces and moments produced by both flapping wings and including the body of the fruit fly as it hovers and then executes a saccade maneuver. The *feflo* incompressible flow solver described briefly above is used to compute the unsteady 3-D flow. The kinematics of the body and the wings

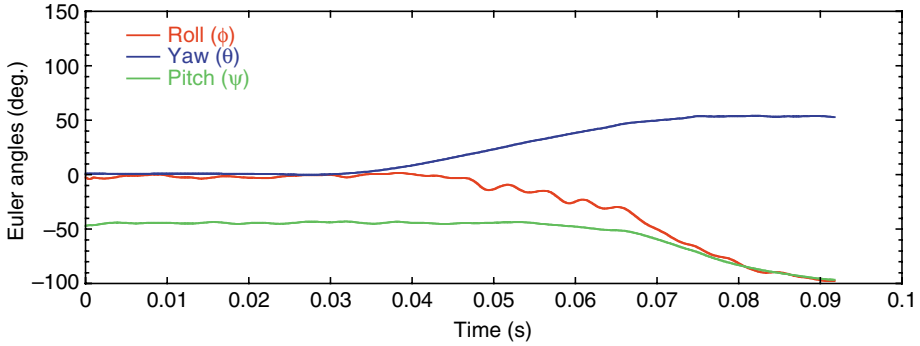

Fig. 3. Roll, yaw and pitch sequence of angular rotations of the body.

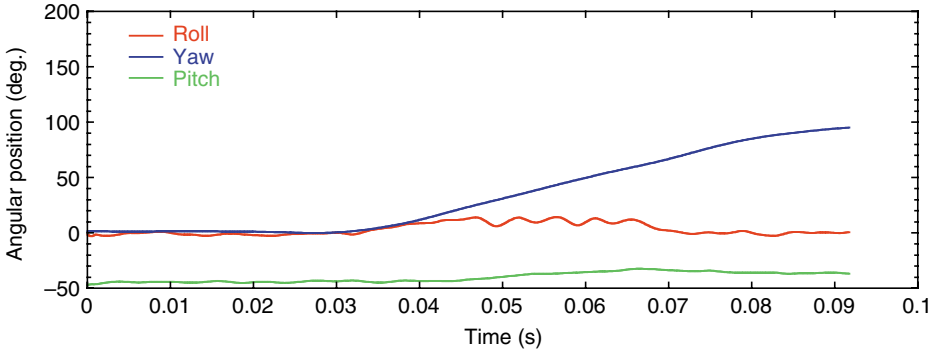

Fig. 4. Angular position of the body during the maneuver.

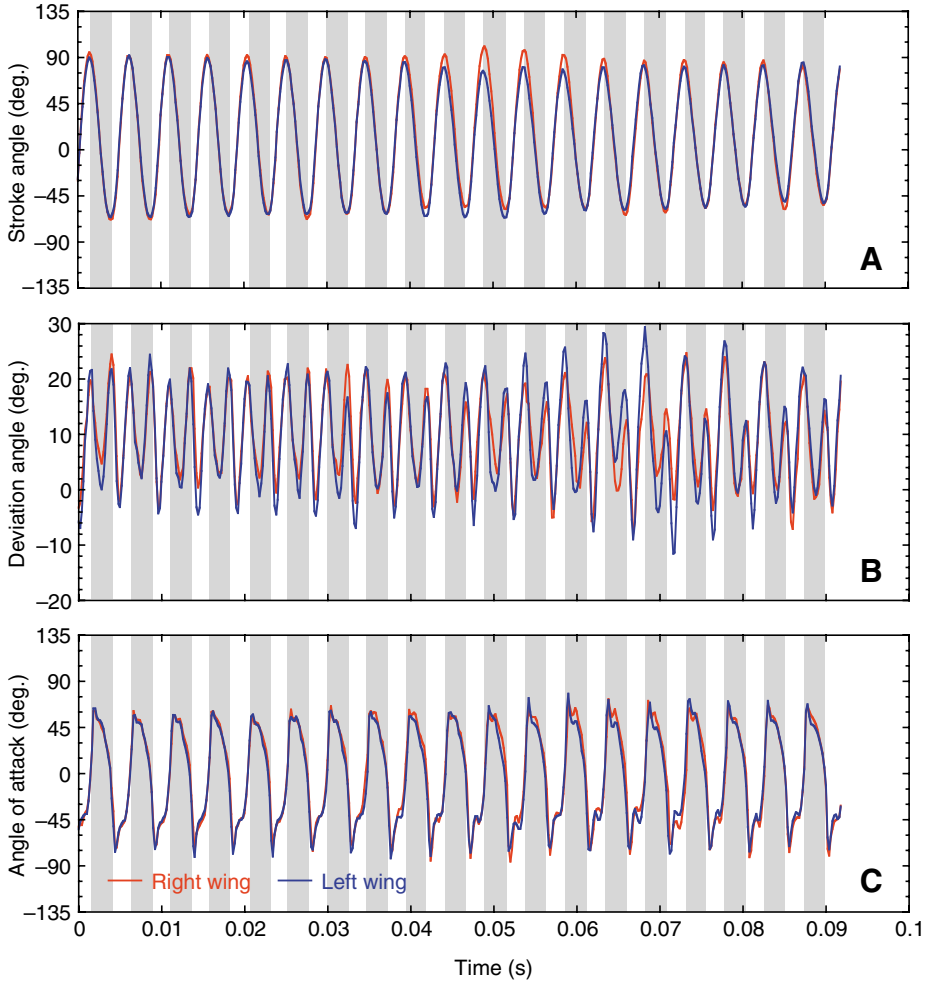

Fig. 5. Angular positions of the wings during the maneuver (from Fry et al., 2003). (A) Stroke angle, (B) deviation from the stroke plane and (C) the angle of attack.

obtained from the experiments of Fry et al. (Fry et al., 2003) are prescribed in this study. The first step in the simulation is to convert the experimentally observed kinematics to rigid body translations and rotations in the computational frame.

Kinematics of the maneuver

Fig. 1 shows the hovering *Drosophila* in the experimental coordinate system (XYZ). The prescribed data consist of the coordinates of the head, the tail, the wing hinges and tips and the unit vector normal to the wings. In order to convert this data to rigid body translation and rotation, first the fruit fly body is placed in the computation coordinate system (*xyz*) with the head to tail aligned along the *x*-axis, the two wings placed flat on the (*y*-*z*) plane, as shown in Fig. 2.

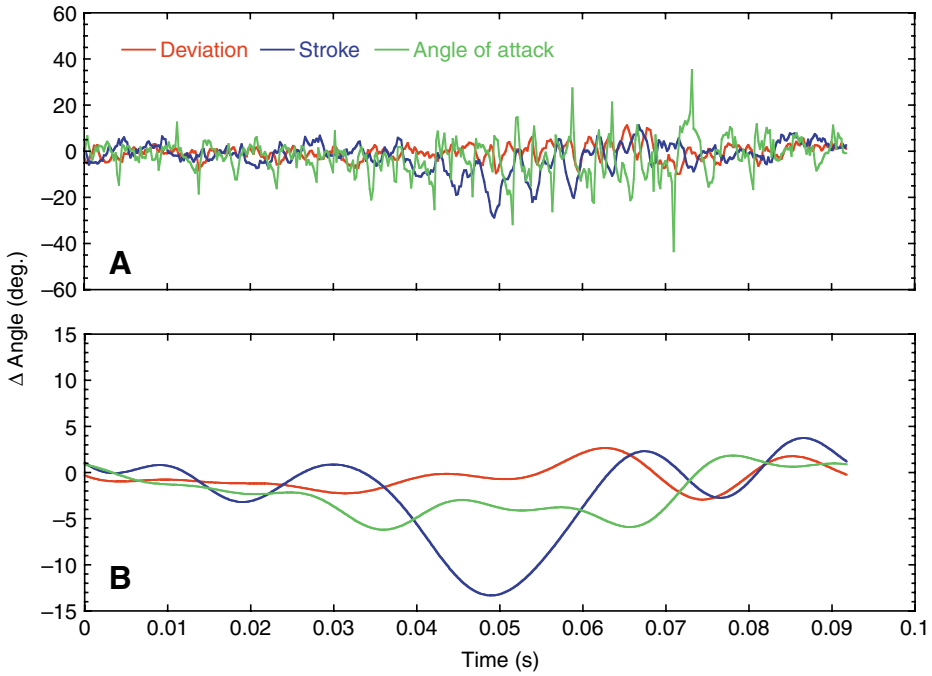

Fig. 6. Difference in angular positions between the wings during the maneuver. (A) Experimental raw data and (B) filtered data.

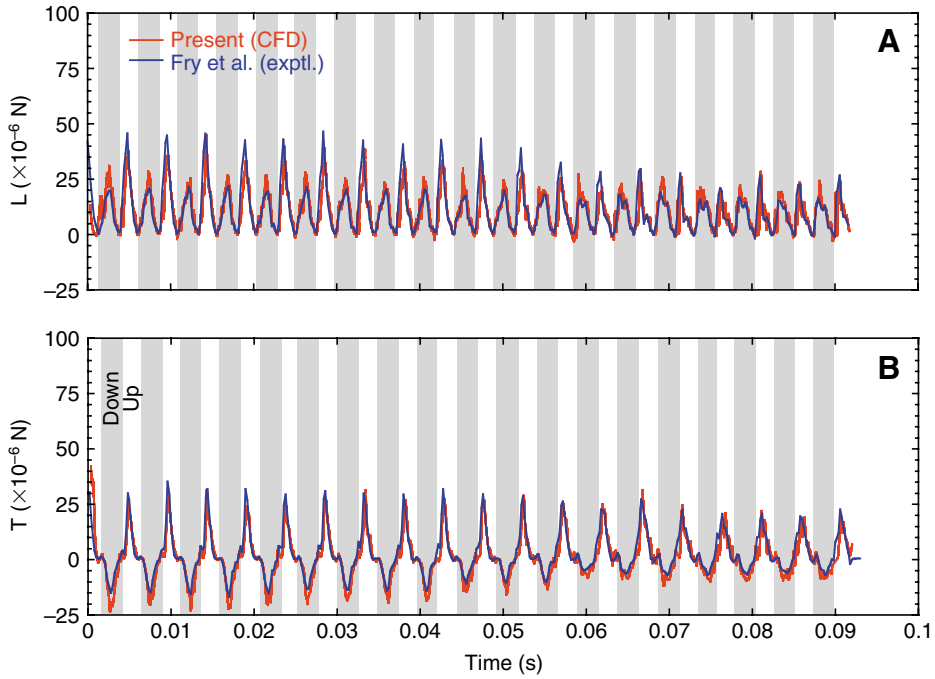

Fig. 7. Comparison of time history of (A) lift (L) and (B) thrust (T) forces. Gray and white bars indicate downstroke and upstroke, respectively.

The body of the fruit fly in Fig. 2 is rotated along the x-axis through a roll angle ϕ, followed by a yaw rotation of θ about the y-axis, and the by a pitch rotation of ψ about the z-axis. This set of rotations is equivalent to the Euler angle systems commonly used in aeronautical engineering. The coordinate transformation for this set of rotations is given elsewhere (Greenwood, 1987) and is as follows.

$$\begin{Bmatrix} X \\ Y \\ Z \end{Bmatrix} = \begin{bmatrix} \cos\psi\cos\theta & \cos\psi\sin\theta\sin\phi - \sin\psi\cos\phi & \cos\psi\sin\theta\cos\phi + \sin\psi\sin\phi \\ \sin\psi\cos\theta & \sin\psi\sin\theta\sin\phi + \cos\psi\cos\phi & \sin\psi\sin\theta\cos\phi - \cos\psi\sin\phi \\ -\sin\theta & \cos\theta\sin\phi & \cos\theta\cos\phi \end{bmatrix} \begin{Bmatrix} x \\ y \\ z \end{Bmatrix}. \quad (3)$$

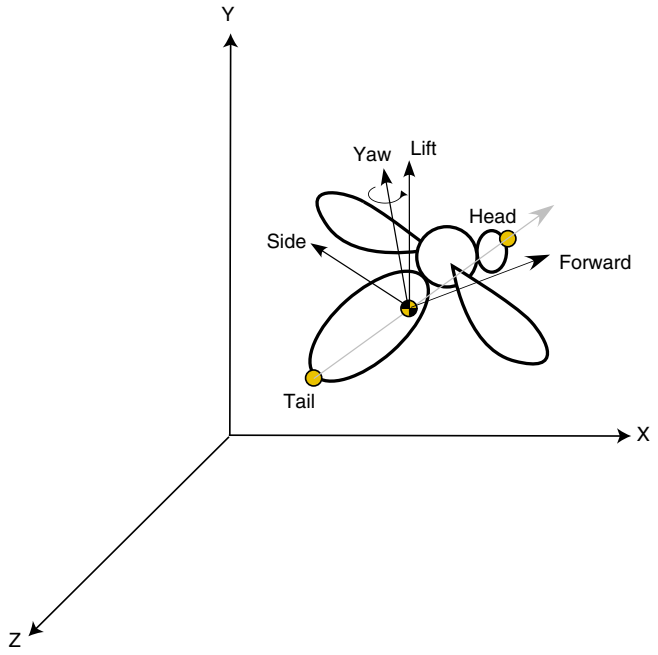

Fig. 8. Force component and yaw axis directions for a maneuvering *Drosophila*.

The rotation angles for the body are obtained from the body–tail vector, the right wing hinge to the left wing hinge (RWH–LWH) vector and the vector orthogonal to these two vectors, as shown in Fig. 3. Examination of the computed Euler angles show that the yaw angle reaches a maximum of 53°, while the pitch and roll angles reach a value close to 90° at the end of the maneuver. Although these are a consistent set of angles, the actual yaw, pitch and roll angles of the fly body can be obtained by pitch and yaw angles from the body–tail vector and then obtaining the roll angle from the RWH–LWH vector. This set of angles is shown in Fig. 4, where the fly is seen to yaw 90° and the pitch remains between 40° and 50° and the roll is nearly zero.

The rotation angles for the wings are obtained from the vectors from the wing hinges (RWH and LWH) to the wing tips (RWT and LWT) and the wing normal vectors (RWN and LWN), e.g. RWH–RWT and RWN vectors shown in Fig. 1. For this purpose, the body is pitched at an average pitch angle of 44.4° obtained over the first 6 hover cycles. The resulting stroke angle (θ), the deviation from the x–z plane (ψ) and the angle of attack (ϕ) of the wings are shown in Fig. 5. The stroke angles of the right and left wings are similar during hover, t=0.0–0.03 s, and towards the end of the saccade maneuver, t=0.07 s onwards, and differ considerably during the saccade, as seen in Fig. 5A. A similar trend in the deviation and angle of attack is shown in Fig. 5B,C. In order to see the differences in the angles between the two wings, the instantaneous differences of these angles were plotted in Fig. 6A. From this figure it can be seen that the differences vary during each wing beat cycle and no clear trend is observed. Hence, these differences were filtered using an fft-filter and the results plotted in Fig. 6B. It is clear that the stroke angle undergoes the largest change during the maneuver. The left wing lags the right wing by approximately 13° midway during the saccade, at t=0.05 s approximately, and recovers at the end of the maneuver. The difference in the angle of attack between the two wings shows that the left wing is maintained at a smaller angle of attack by approximately 6° throughout the maneuver. The difference in the deviation angle of the right and left wings shows that the right wing is at a slightly higher elevation angle during the maneuver.

Unsteady computations of forces and moments

Using the kinematics described above, the unsteady flow over a maneuvering fruit fly was computed using the incompressible flow solver. The instantaneous surface pressure distribution on the wings and the body of the fruit fly was integrated to produce the time history of forces. These forces were resolved in the y-direction to yield the lift force and the resultant of the force in the x- and z-directions along the tail–head vector to yield the forward horizontal force.

The results are shown in Fig. 7 and are compared with the experimentally obtained forces of Fry et al. (Fry et al., 2003). The comparison shows that the computed results agree extremely well with the experiments throughout the maneuver. From Fig. 7A, it is clear from the experimental measurements that the lift peaks during the upstroke are almost twice as large as the peaks during the downstroke during hovering and in the initial period of the saccade maneuver, from t=0.0 to 0.05 s. At the beginning of the saccade, the computed lift during the downstroke is higher than the measured lift while the computed lift on the upstroke is slightly less than the measured lift. During the later part of the maneuver, the peak in the lift force drops in the upstroke part of the cycle and the peak during the downstroke remains similar to the pre-saccade value. The computed lift is very close to the measured lift, on both the upstroke and the downstroke, as the saccade maneuver progresses. The thrust force peaks to a value of nearly 25 μN during the upstroke during the hover and early stages of the saccade and decreases during the later part of the maneuver. The computed thrust and drag force time history is nearly identical to the measured thrust throughout the entire maneuver. The peak drag force during the downstroke decreases continuously during the maneuver.

The yaw moment experienced by the fruit fly during the maneuver is computed about the mid point between the head and tail along an axis normal to the head–tail vector and the right wing hinge to the left wing hinge vector, shown in Fig. 8. The contributions of the yaw moment from the right and left wings are shown in Fig. 9A. It is clear that most of the yaw moment is created during the upstroke and the two wings produce moments in the opposing direction, as would be expected. The mean moment created by the right wing is slightly larger that that of the left wing producing a net yaw moment. Fig. 9B shows the total instantaneous yaw moment created by the right and the left wings. This plot does not show any continuous yaw moment production during the saccade

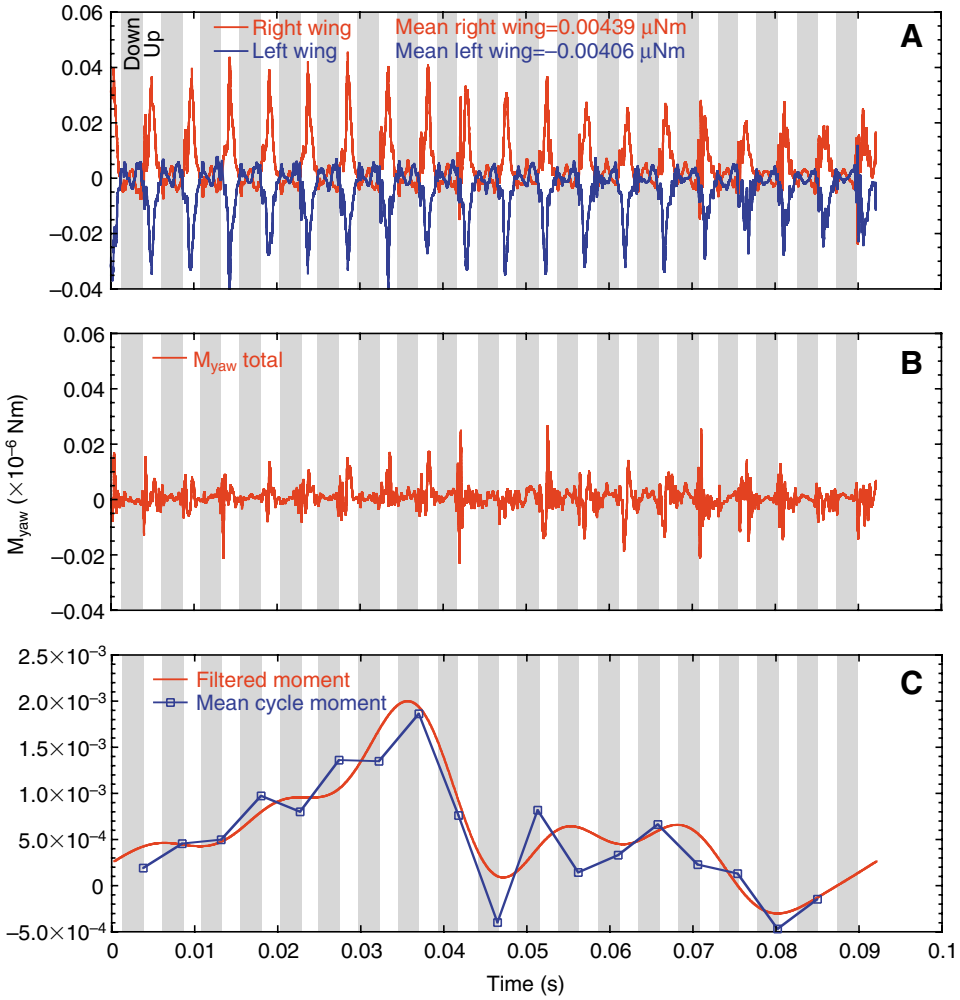

Fig. 9. Time history of yaw moment M_{yaw}. (A) Contributions from right and left wings, (B) the total moment and (C) the filtered moment.

maneuver, t=0.03–0.07 s, although there are instants where the net yaw moment is large, e.g. t=0.042 s, 0.052 s and 0.07 s. Also, it can be seen that the yaw moment is relatively small during the downstroke compared to the large excursions during the upstroke. This total yaw moment is then filtered through an fft-filter and the result is shown in Fig. 9C. The yaw moment continuously increases during the pre-saccade period and reaches a maximum value of 2×10^{-9} Nm at t=0.03 s, and a local maximum of 5×10^{-10} Nm between t=0.05 s and 0.07 s. This yaw moment behavior is very similar to the torque production described by Fry et al. (Fry et al., 2003). The experimental torque shown in fig. 3C of Fry et al. (Fry et al., 2003) was been obtained using a low pass filter and averaging over six species. The use of an fft-filter can be justified by the fact that the fruit fly torque is dominated by the inertia (Fry et al., 2003). Moreover, the body of the fruit fly may not be able to respond to the instantaneous changes in forces and moments at the flapping frequency of the wings. Hence, in this study the data was filtered with a maximum frequency of 60 Hz, and both raw data and filtered data are presented. The mean yaw moment during each cycle is also shown in Fig. 9C and is very similar in both magnitude and trend compared to the filtered moment. The filtering process used here seems to be a method to obtain the mean cycle values without the knowledge of beginning and end of each flapping cycle.

Origin of the yaw moment

In order to find the origin of this yaw moment, the force vector acting on each wing is decomposed into its forward, lift and sideways components. For this purpose, the forward direction is taken to be the vector from tail to head of the insect and parallel to the x–z plane, as shown in Fig. 8. The lift is in the direction normal to the flight and is aligned along the y-axis, i.e. the vertical component of force. The sideways direction is then defined orthogonal to the lift and forward directions.

Fig. 10A shows the forward component of the computed forces produced by the wings during the entire maneuver. During hovering, the thrust produced during the upstroke is nearly anti-symmetric to the force produce during the downstroke and the contributions from the right and left wings are nearly the same. During the saccade, t=0.03 s–0.07 s, there is a considerable

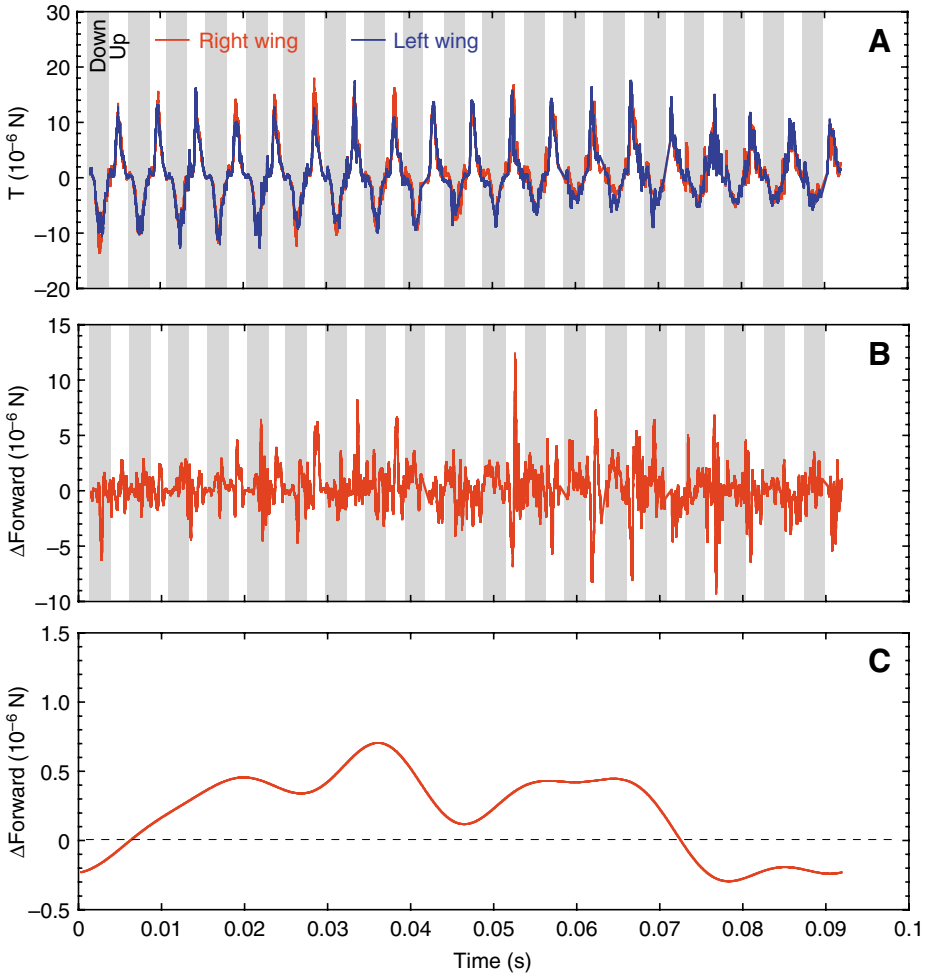

Fig. 10. Time history of forward force produced by the wings. (A) Contributions from right and left wings, (B) the difference in force and (C) the filtered difference in force.

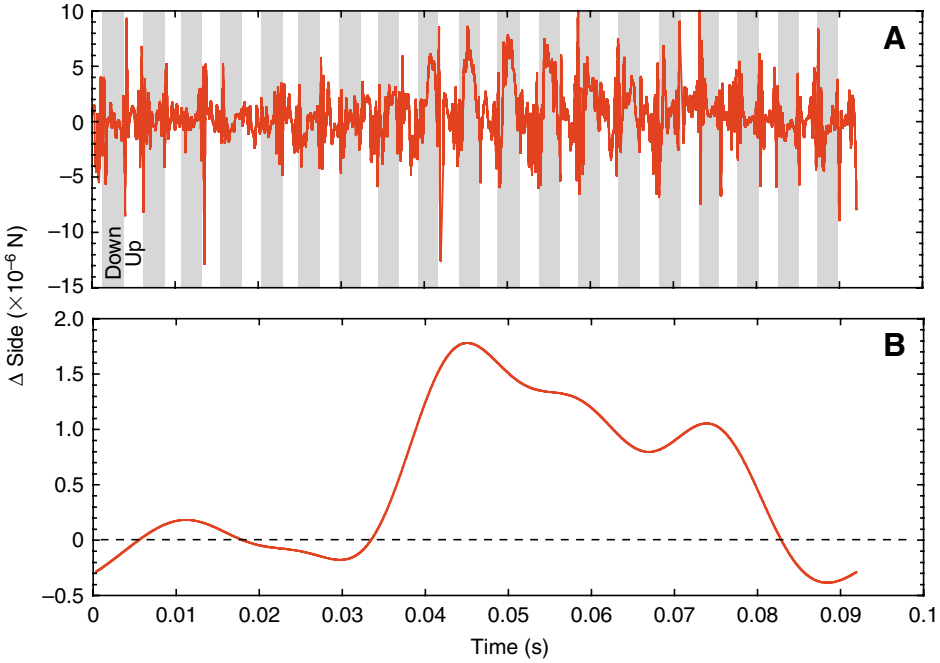

Fig. 11. Time history of (A) differential side force and (B) filtered side force.

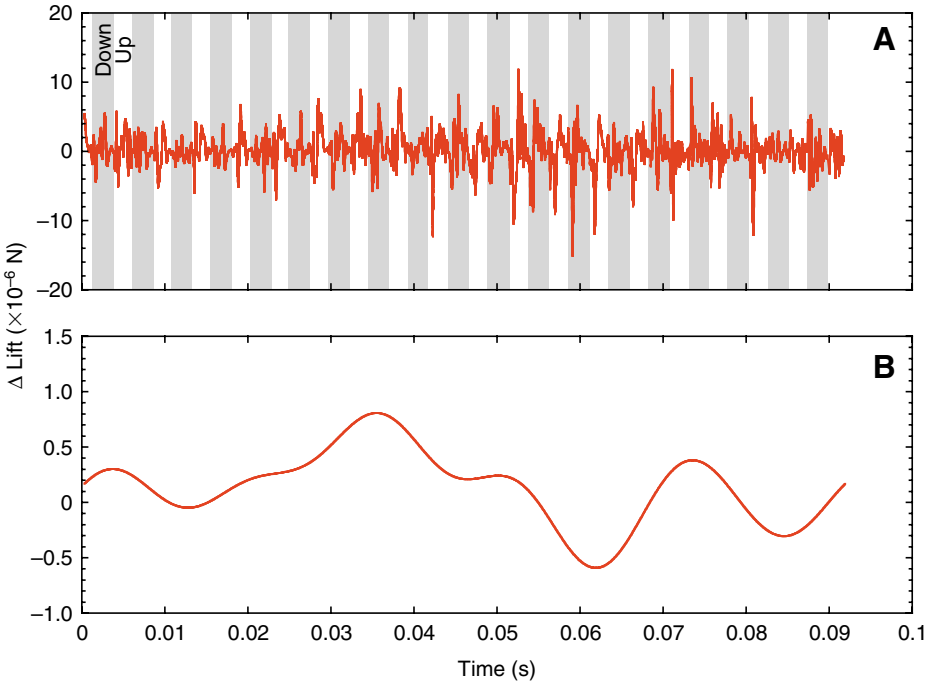

Fig. 12. Time history of (A) differential lift force and (B) filtered lift force.

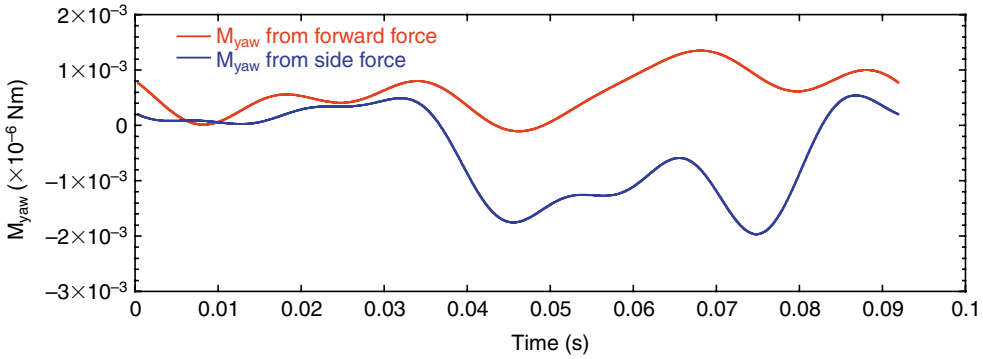

Fig. 13. Contributions of the forward and side forces to the yaw moment M_{yaw}.

increase in the thrust produced during the upstroke compared to the drag produced in the downstroke, and the right wing produces slightly larger thrust. Fig. 10B shows the difference in the thrust produced by the right and the left wings and exhibits both positive and negative values. Hence, this difference in the forward force is further filtered and is shown in Fig. 10C. From this figure it is clear that the right wing produces additional forward force compared to the left wing during the saccade maneuver. The differences in the sideways and lift components of the forces between the right and left wings were filtered in a similar manner and are shown in Figs 11 and 12. The differential side force component remains positive during the maneuver with a peak value of 1.78 μN at the beginning of the maneuver, t=0.045 s in Fig. 11B, compared with a peak value of 0.8 μN at t=0.035 s in Fig. 12B, and therefore could contribute to the yaw moment. The differential lift force is positive in the initial period of the maneuver and becomes negative in the later half of the maneuver.

In order to find out what the contribution of each of these force components is to the yaw moment, the corresponding moment arms have to be determined from the center of pressure. Fig. 13 shows that the forward force has a positive contribution to the yaw moment during the entire maneuver and the contribution from the side force is positive during the initial phase of the turning and remains negative during the rest of the maneuver, thus providing a restoring torque. The remainder of the yaw moment arises from the lift force acting in the y-direction, resulting in a non-zero component of moment along the yaw axis.

Fig. 14A,B show the length of the moment arms for the forward and side forces, respectively. These moment arms were obtained from the center of pressure (CP) for each wing and computing the distances of these CP to the center of rotation

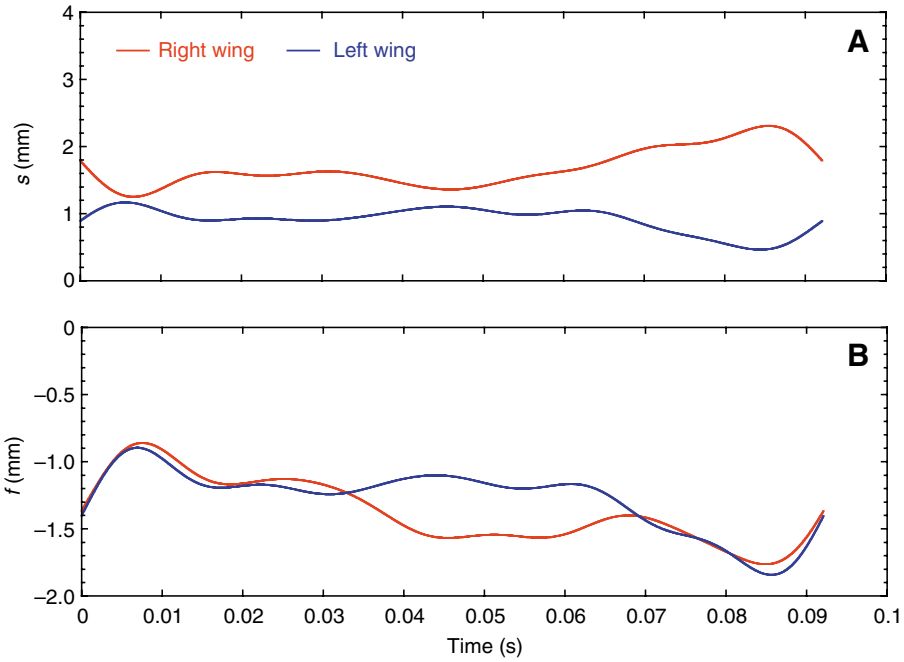

Fig. 14. Moment arms for (A) the forward (*f*) force and (B) side (*s*) forces.

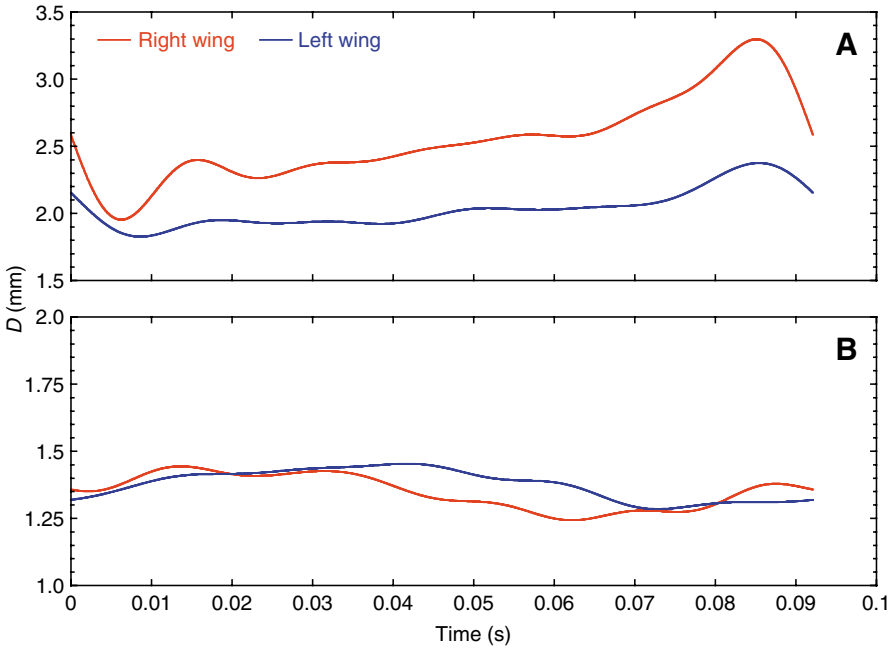

Fig. 15. Distance (*D*) of the center of pressure from (A) the center of rotation and (B) the wing hinge.

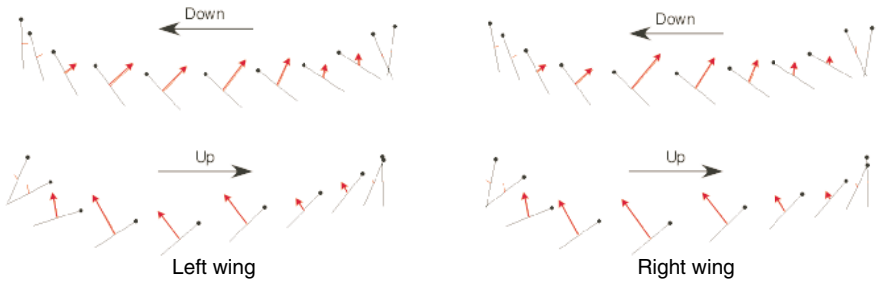

Fig. 16. Force vectors (red arrows) on the left and right wings during a hover cycle, *t*=0.0156 s to 0.0204 s.

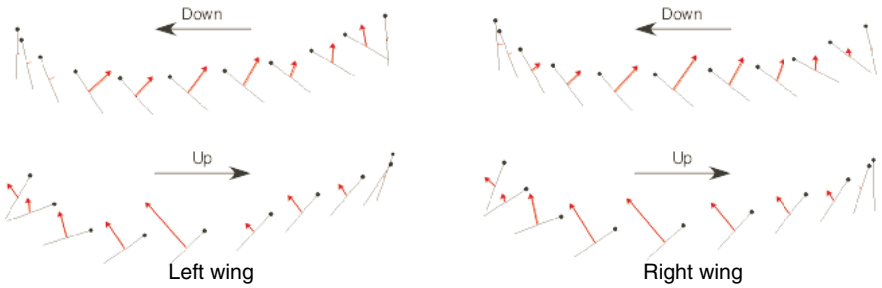

Fig. 17. Force vectors (red arrows) on the left and right wings at the beginning of the saccade, t=0.0298 s to 0.0346 s.

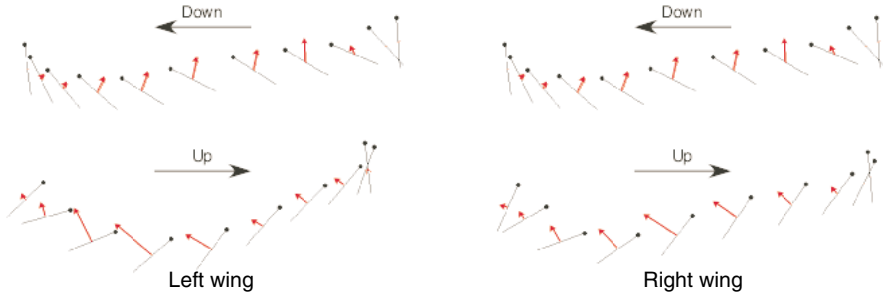

Fig. 18. Force vectors (red arrows) on the left and right wings in the middle of the saccade, t=0.0538 s to 0.0586 s.

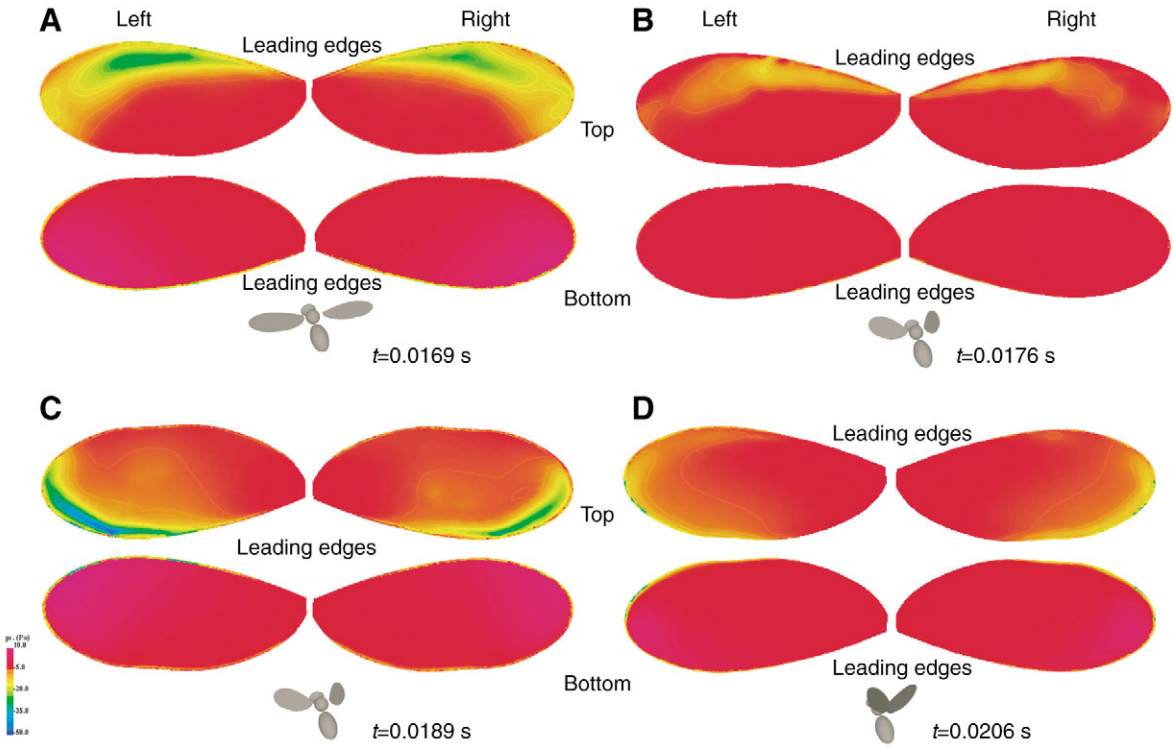

Fig. 19. Surface pressure contours on the wings during a hover cycle.

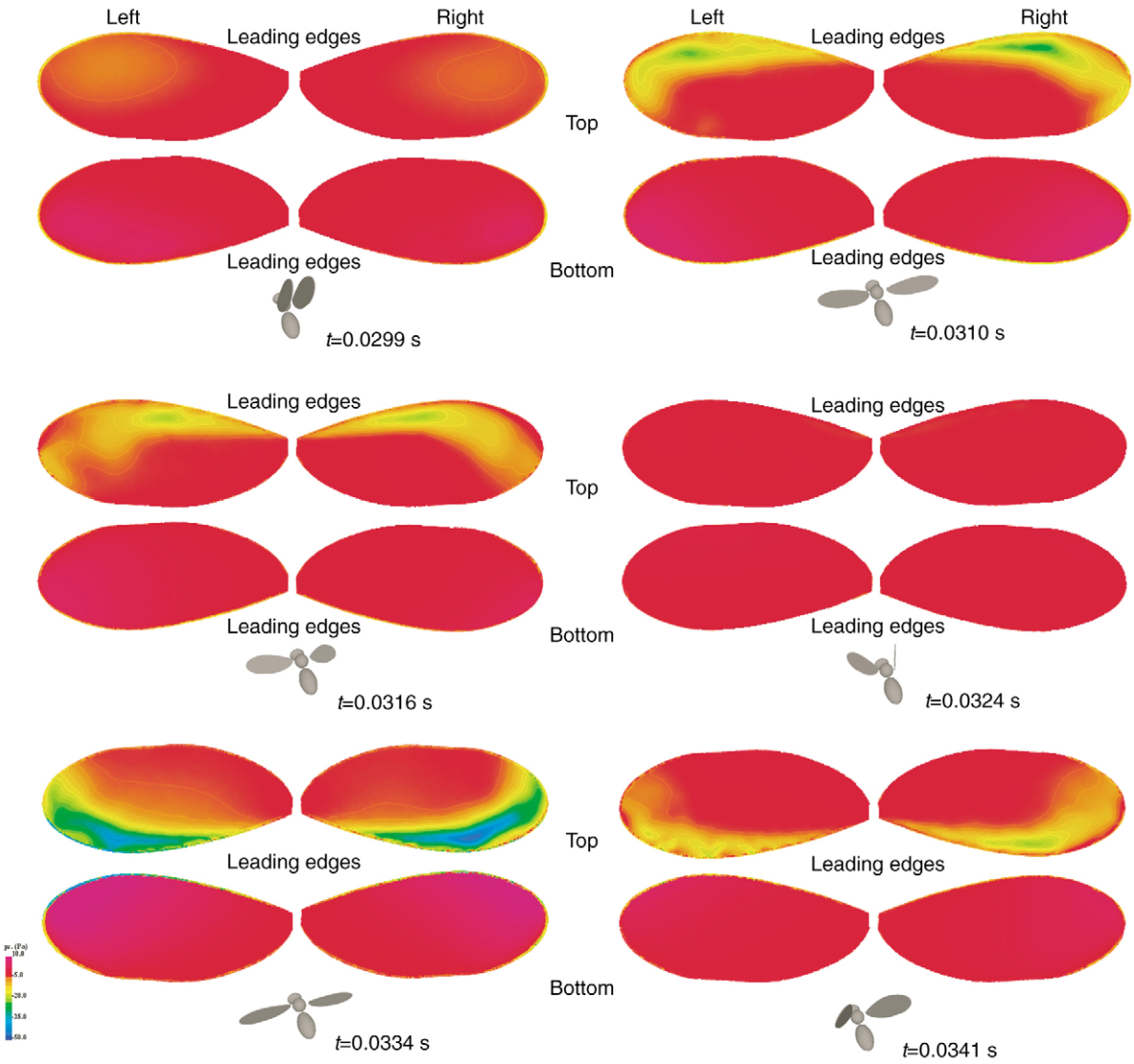

Fig. 20. Surface pressure distributions during the initial phase of the saccade maneuver. Colour key as in Fig. 19.

along the side and forward directions, shown in Fig. 8. From Fig. 14A, it can be seen that the center of pressure for the right wing is located away from the center along the side ways direction throughout the maneuver.

The moment arm for the sideways force component, Fig. 14B, shows that the center of pressure is located between the center of rotation and the tail of the fruit fly, and is indicated by the negative values of the moment arm. Further, during hovering the location of the center of pressure nearly coincides between the right and left wings, hence reducing the contribution due to the side force.

During the later phases of the saccade, the moment arm of the right wing is larger in magnitude thus producing the restoring negative torque. Fig. 15A shows the distance of the center of pressure from the center of rotation for each wing. The center of pressure for the right wing is located at nearly 2.5 mm from the center of rotation midway between the head and tail of the insect and that of the left wing is at 2.0 mm throughout the saccade. Fig. 15B shows the location of the center of pressure from the wing hinges along the spanwise direction. This distance is nearly constant at 1.4 mm throughout the maneuver, which is 60% of the span of the wing.

Force production and surface pressures during 3 typical cycles

Fig. 16 shows the wing motion and the force vectors generated by the wings during a typical hover cycle. The wing motion shown by the leading edge dot and the orientation of the chord shows a symmetric or U-shaped profile both during the downstroke and upstroke. The motion is similar for the right and left wings. The force production is also similar during this cycle as expected. The force vector shown in here is the resultant of the lift and the thrust components and does not include the side force component.

At the beginning of the saccade maneuver, the wing motion changes from the symmetric shape to a ‘banana-shape’ during

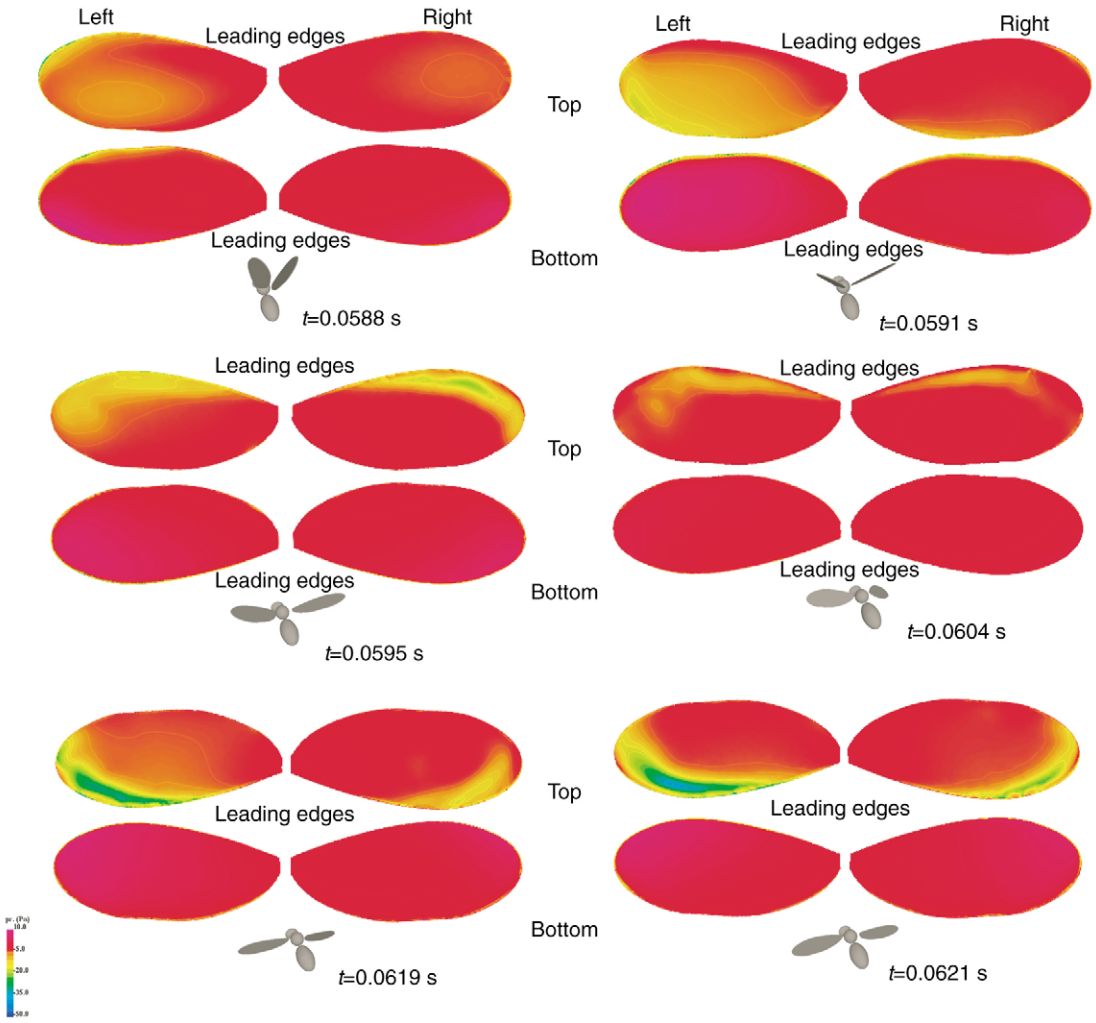

Fig. 21. Surface pressure distributions during the middle of the saccade maneuver. Colour key as in Fig. 19.

the downstroke and the upstroke remains relatively symmetric, as shown in Fig. 17. The forces on the two wings also show differences, the right wing producing larger force during the downstroke and the later half of the upstroke.

During the middle of the saccade maneuver, the wing motion shows an asymmetric banana-shaped profile both during up and downstrokes, Fig. 18, with the right wing showing a more pronounced turning at stroke reversal. Also, the stroke angle for the right wing is considerably larger compared to the left wing. The magnitudes of the force vector on the left wing for this cycle is slightly larger than that of the right wing.

Fig. 19 shows the pressure distribution on the surface of the wings during a hover cycle and is almost symmetric between the right and left wings. Hence, the forces produced by the wings are also symmetric. At an instant midway during the downstroke, t=0.0169 s shown in Fig. 19A, the lift achieves a maximum. At this instant, a low-pressure region is visible on the top of the wings and a high-pressure region is present on the bottom of the wings. At t=0.0176 s, just before stroke reversal shown in Fig. 19B, a small low pressure region is visible on the top of the wings in the leading edge region and at mid span. The pressure on the bottom of the wings is nearly constant at this instant. Fig. 19C shows the pressure distribution midway during the upstroke with a high-pressure region on the lower side of the wing. The extent of the high-pressure region is larger and the suction pressure is lower compared to the middle of the downstroke, leading to a higher lift on the upstroke. Fig. 19D shows the pressure distribution just after stroke reversal and is nearly symmetric between the right and left wings leading to a force vector opposing each other.

Fig. 20 shows the pressure distribution during the first cycle of the saccade maneuver. At t=0.0299 s, the force vectors oppose each other and with the wings aligned nearly in the vertical direction producing zero lift. The pressure distributions on the right and left wings do not exhibit any symmetry during this cycle with the bottom left wing showing higher pressure extending over a larger region. At midway through the downstroke, t=0.0310 s, a maximum lift is produced. At stroke reversal, the pressure is nearly constant on the bottom of the wing at t=0.0324 s. At t=0.0334 s, the lift produced reaches a peak. The instantaneous yaw moment

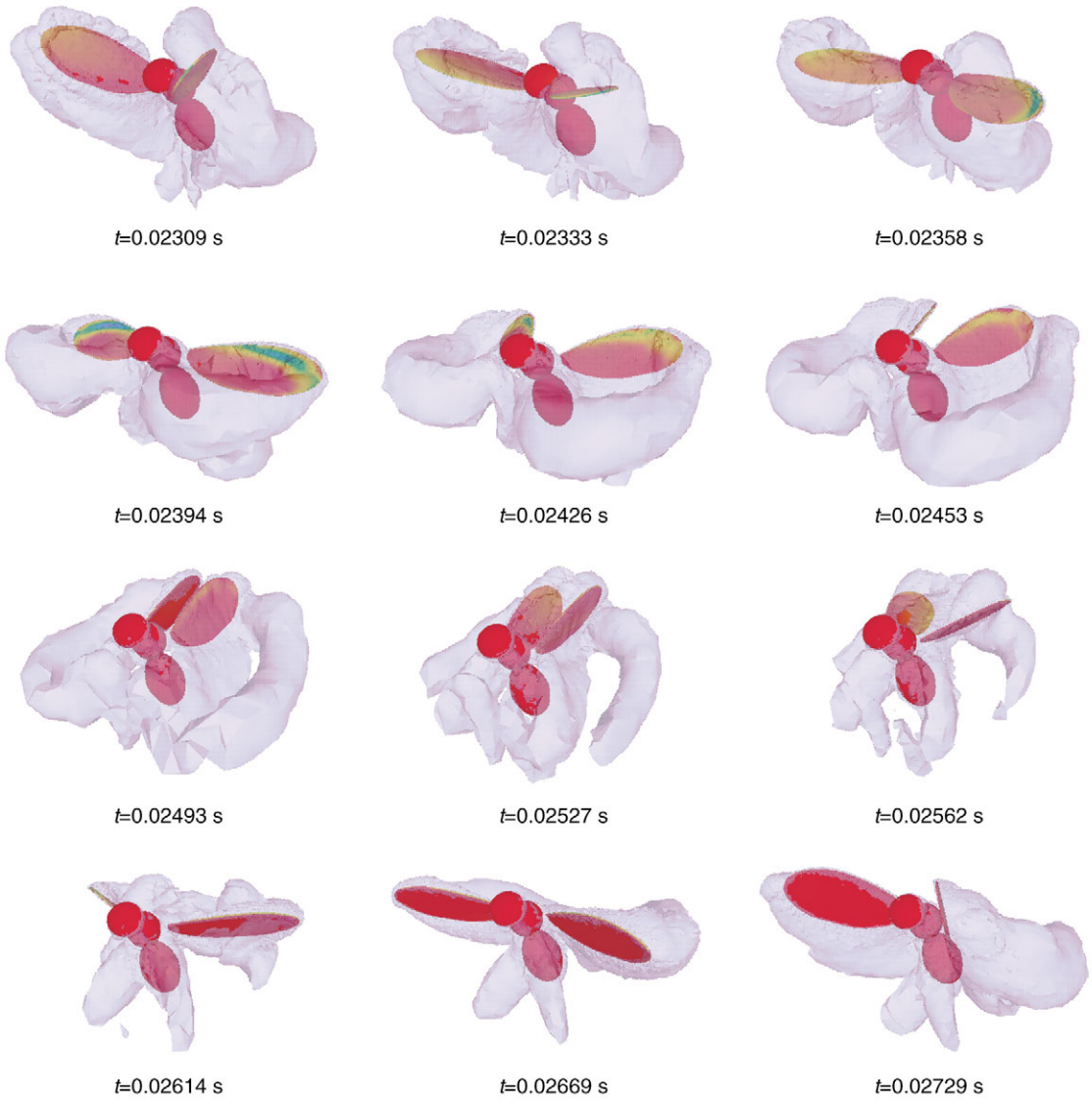

Fig. 22. Vorticity generated by the leading and trailing edges of the wings shown by iso-vorticity surface during a hover cycle.

also reaches a peak at this time. The lift and the thrust produced reduce toward the end of the cycle, close to stroke reversal at t=0.0341 s. The yaw moment produced during the downstroke is nearly zero for each of the wings whereas during the middle of the upstroke the yaw moment reaches an appreciable value, albeit the left wing producing a negative moment opposing the right wing.

During a cycle in the middle of the maneuver, the asymmetries in the wing positions and the pressure distributions can be seen in Fig. 21. At t=0.0591 s and at t=0.0619 s, the lift produced attains a peak during the downstroke and the upstroke, respectively. At t=0.621 s, a maximum thrust is produced during the upstroke.

Vorticity evolution during hover and saccade cycles

Fig. 22 shows the sequence of evolution of the vorticity generated by the leading and trailing edges of the wings during a hover cycle. At t=0.2309 s, at stroke reversal we see vortices generated from the leading and trailing edges. At t=0.0233 s the vortices from the trailing edges are pulled up due to the wing motion and continue to get stretched at t=0.02358 s where they form an arch-like structure below the head. At t=0.02394 s, the wings are in the middle of the upstroke with the vortex from the leading edge forming a loop as the wing sweeps back to a position close to stroke reversal at t=0.02453 s. At stroke reversal, t=0.02493 s, the arch-like vortices that were shed at the end of the previous downstroke are pronounced and soon after reversal, this structure pinches off of the loop, t=0.02527 s, forming a Λ-like structure, which follows downstream until t=0.02729 s. Fig. 23 shows this evolution viewed from the back of the hovering fruit fly. At t=0.02233 s, the Λ-like structure connected to the loop can be seen. At t=0.02309 s, the arch pinches off from the loop and at t=0.02333 s, this arch joins the Λ-structure from the front and

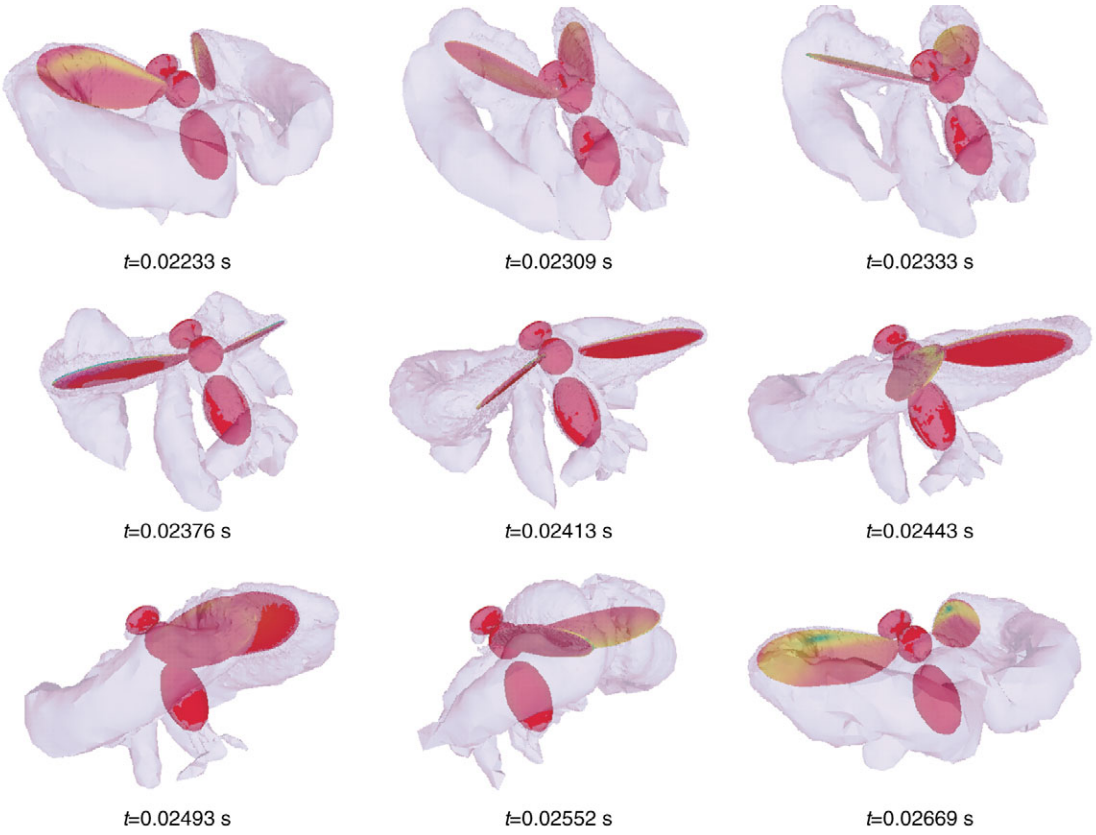

Fig. 23. Iso-vorticity surfaces as seen from the back of the fruit fly during hover.

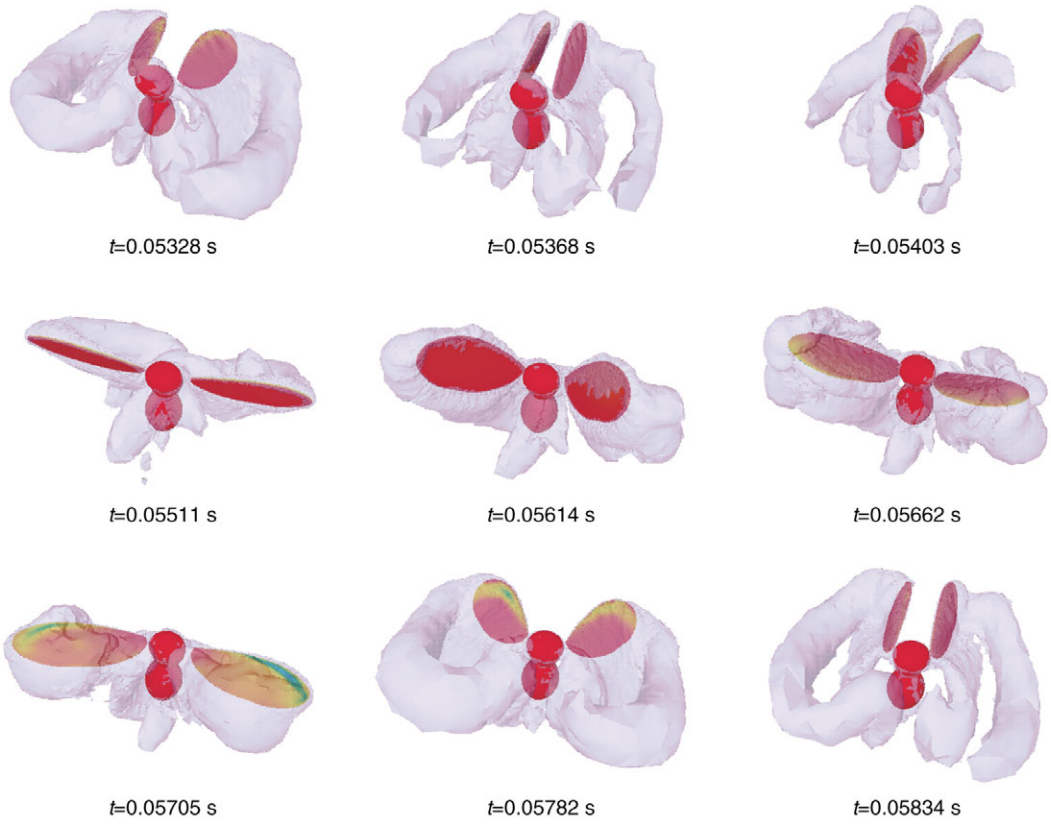

Fig. 24. Contours of iso-vorticity shed by the fruit fly during saccade maneuver.

pinches off from it at t=0.02376 s. Between t=0.02413 s and 0.02493 s, the wing is executing the upstroke producing the loop structure and at t=0.02552 s, just after stroke reversal, we can see the Λ-like structure emerging.

Fig. 24 shows the evolution of vorticity shed from the wings through one cycle in the middle of the saccade maneuver. The vortex loops shed from the leading edge and the wing tip clearly show asymmetry between the right and left wings. The loop ahead of the body on the right wing is still connected at t=0.05328 s while on the left side it has already pinched off. We can see the vortex shedding off the leading edge at stroke reversal, t=0.05403 s, and being made into a loop through the downstroke. At t=0.55–0.57 s, we can see the Λ-like structure generated from the previous upstroke. This structure, in contrast to the hover cycle exhibits asymmetry in the lengths of the legs mainly since the leg on the left side is formed due to an earlier pinching off compared to the right side. At the stroke reversal, t=0.05662 s, we see the leading edge vortex being shed and drawn into a loop throughout the upstroke.

Summary and conclusions

3-D unsteady computations of a maneuvering fruit fly *Drosophila* have been carried out. The kinematics of the wings and the body were obtained from experimental observations and converted to 6-DOF motion for the body and the wings. The unsteady force and moments *via* direct integration of the pressure on the surfaces were obtained and compared to the experimental results and show excellent agreement for the entire hover and saccade maneuver, consisting of over 20 wing beat cycles. The kinematics of the wings show that subtle changes can result in the yaw moment required to perform the turning maneuver. During the maneuver, the largest change between the right and the left wings occurred in the stroke angle. The left wing lagged the right wing by approximately 13° midway during the saccade, at approximately t=0.05 s and recovered at the end of the maneuver. The difference in the angle of attack between the two wings shows that the left wing was maintained at a smaller angle of attack by approximately 6° throughout the maneuver. The difference in the deviation angle of the right and left wings show that the right wing was at a slightly higher elevation angle during the maneuver. These subtle changes in the kinematics can be incorporated for controlling unconventional vehicles such as the Biplane Insectoid Travel Engine (BITE) being developed at the Naval Research Laboratory.

The yaw moment reached a peak value at the beginning of the maneuver, remained positive throughout the remainder of the maneuver, and exhibited a restoring moment after the maneuver. The origin of the yaw moment was investigated by computing the center of pressures on each wing and the individual moment arms. This showed that the forward force and a component of the lift force produced the turning moment while the side force produced the restoring torque during the maneuver. The vorticity shed from the wing leading edge and the tips shows a loop-like structure, which during stroke reversals pinched off into Λ-like structures that were advected downstream. The role of these vortex structures on the force production mechanism is being investigated.

This work was supported by ONR through an NRL 6.1/6.2 project: ‘Flapping Propulsion for Unconventional MAVs’, with Dr James Kellogg as the project monitor. The valuable discussions and the information on the experimental kinematics with Dr Steven Fry of the Institute of Neuroinformatics, Zürich, Switzerland are greatly appreciated. Also, regular discussions with Dr Rainald Löhner of George Mason University is greatly appreciated. This work was supported in part by a grant of HPC time from the DoD HPC centers, ARL MSRC SGI-O2K and NRL SGI-O2K.

References

Dickinson, M. H., Lehmann, F.-O. and Sane, S. P. (1999). Wing rotation and the aerodynamic basis of insect flight. *Science* **284**, 1954-1960.

Fry, S. N., Sayaman, R. and Dickinson, M. H. (2003). The aerodynamics of free-flight maneuvers in Drosophila. *Science* **300**, 495-498.

Greenwood, D. T. (1987). *Principles of Dynamics*. Englewood Cliffs, NJ: Prentice-Hall.

Jones, K. D. and Platzer, M. F. (2003). Experimental investigation of the aerodynamic characteristics of flapping-wing micro air vehicles. *AIAA-2003-0418*, Washington, DC.

Kellogg, J., Bovais, C., Cylinder, D., Dahlburg, J., Foch, R., Platzer, M., Ramamurti, R. and Sandberg, W. C. (2001). Non-conventional aerodynamics for micro-UAVs. Proceedings of the 16th International UAV Systems Conference, Bristol, UK.

Kellogg, J., Bovais, C., Foch, R., Cylinder, D., Ramamurti, R., Sandberg, W. C., Gardner, J., Srull, D., Piper, G. and Vaiana, P. (2003). Development and testing of unconventional micro air vehicle configurations, *AIAA-2003-6356*, Washington, DC.

Liu, H. and Kawachi, K. (1998). A numerical study of insect flight. *J. Comput. Phys.* **146**, 124-156.

Ramamurti, R. and Löhner, R. (1992). Evaluation of an incompressible flow solver based on simple elements. In *Advances in Finite Element Analysis in Fluid Dynamics*. FED Vol. 137 (ed. M. N. Dhaubhadel, M. S. Engleman and J. S. Reddy), pp. 33-42. New York: ASME Publication.

Ramamurti, R. and Sandberg, W. C. (2002). A three-dimensional computational study of the aerodynamic mechanisms of insect flight. *J. Exp. Biol.* **205**, 1507-1518.

Ramamurti, R., Löhner, R. and Sandberg, W. C. (1994). Evaluation of a scalable 3-D incompressible finite element solver. *AIAA-94-0756*, Washington, DC.

Ramamurti, R., Löhner, R. and Sandberg, W. C. (1995). Simulation of a torpedo launch using a 3-D incompressible finite element flow solver. *AIAA-95-0086*, Washington, DC.

Ramamurti, R., Löhner, R. and Sandberg, W. C. (1999). Computation of the 3-D unsteady flow past deforming geometries. *Int. J. Comput. Fluid Dyn.* **13**, 83-99.

Ramamurti, R., Sandberg, W. C., Löhner, R., Walker, J. A. and Westneat, M. W. (2002). Fluid dynamics of flapping aquatic flight in the bird wrasse: 3-D unsteady computations with fin deformation. *J. Exp. Biol.* **205**, 2997-3008.

Ramamurti, R., Sandberg, W. C. and Löhner, R. (2004). The influence of fin rigidity and gusts on the force production of fishes and insects: a computational study. *AIAA-2004-0404*, Washington, DC.

Ramamurti, R., Sandberg, W. C., Vaiana, P., Kellogg, J. and Cylinder, D. (2005). Computational fluid dynamics of unconventional air vehicle configurations. *Aeronaut. J.* **109**, 337-347.

Sun, M. and Tang, J. (2002). Unsteady aerodynamic force generation by a model fruit fly wing in flapping motion. *J. Exp. Biol.* **205**, 55-70.

Walker, J. A. and Westneat, M. W. (1997). Labriform propulsion in fishes: kinematics of flapping aquatic flight in the bird wrasse, *Gomphosus Varius* (Labridae). *J. Exp. Biol.* **200**, 1549-1569.

Willmott, A. P. and Ellington, C. P. (1997). The mechanics of flight in the hawkmoth *Manduca sexta*. II. Aerodynamic consequences of kinematics and morphological variation. *J. Exp. Biol.* **200**, 2723-2745.